

1 **Cloud, Thermodynamic, and Precipitation**  
2 **Observations in West Africa during 2006**  
3  
4  
5  
6  
7  
8  
9  
10  
11  
12

13 Pavlos Kollias<sup>1</sup>, Mark Miller<sup>2</sup>  
14 Karen L. Johnson, Michael Jensen, and David Troyan<sup>3</sup>  
15  
16

- 17 1. Department of Atmospheric and Oceanic Sciences, McGill University  
18 2. Department of Environmental Sciences, Rutgers University  
19 3. Department of Atmospheric Sciences, Brookhaven National Laboratory  
20  
21  
22  
23  
24  
25  
26  
27

28 Corresponding Author:

29 Dr. Pavlos Kollias

30 Department of Atmospheric and Oceanic Sciences

31 805 Sherbrooke Street West

32 Montreal, Quebec H3A 2K6

33 Tel.: 514-398-1500

34 Fax: 514-398-6115

35 Email: pavlos.kollias@mcgill.ca  
36  
37  
38

1

2

## Abstract

3

4 In 2006, the ARM Mobile Facility (AMF) completed a one-year deployment at Niamey,

5 Niger, Africa in support of the Radiative Divergence using AMF, GERB and AMMA

6 Stations (RADAGAST) field campaign, which is the subject of this special issue.

7 Observations from the AMF instrumentation are used to analyze the relationship between

8 clouds, precipitation, and the thermodynamic environment in this rarely observed region.

9 The one-year deployment period enabled measurements in the dry and wet (monsoon)

10 seasons and through the transitions in May and September, respectively. Cirrus clouds in

11 the 10-15 km layer with modest monthly cloud fraction and mean depth of approximately

12 one kilometer are ubiquitous through the observing period as observed in other regions of

13 the tropics. The monsoon season from May to September is characterized by convective

14 clouds of varying depth that produce precipitation of varying intensity, as indicated by

15 cloud radar. Peak surface rainfall is observed during August and the largest daily rainfall

16 rates are observed during the period from July to September. The Lifting Condensation

17 Level (LCL) is observed to decrease as the monsoon season progresses and a strong

18 correlation between the height of the LCL and precipitation is demonstrated. Cooling of

19 the lower troposphere is implicated as the probable cause of the lowering of the LCL.

20 Conversely, the amount of Convective Available Potential Energy is found to be poorly

21 correlated with precipitation. As in other tropical relationships, the height of the zero-

22 degree isotherm is integrally related to the thermodynamic and cloud structure.

23

1

## 2       **1. INTRODUCTION**

3

4   The Sahel region of West Africa has experienced recurring and persistent precipitation  
5   anomalies for at least the past fifty years. Periodicity on the scale of a decade or more is  
6   common and severe droughts have caused extreme societal consequences. A plethora of  
7   mechanisms have been proposed to explain precipitation anomalies (Desbois et al., 1998).  
8   Such mechanisms include feedbacks from changes in surface albedo and soil moisture  
9   (Otterman, 1974; Charney, 1975) and periodic shifts in the large-scale dynamic construct  
10   of the region related to the African easterly jet and sea surface temperatures in the  
11   Tropical Atlantic (Lamb, 1978; Cook, 1999).

12

13   The bulk of the rainfall that is observed in the Sahel is associated with propagating  
14   mesoscale convective complexes and tropical squall lines (Laing and Fritsch, 1993;  
15   Desbois et al., 1988). Several studies have used satellite climatology to show that these  
16   storm complexes often propagate from east to west across the Sahel and are often  
17   associated with tropical easterly waves. Satellite data have also been used to examine the  
18   characteristics of easterly waves, the structure of precipitation-producing complexes, and  
19   climatology and diurnal cycle of clouds in the region. Other studies have employed  
20   model data assimilation techniques used in the initialization of numerical models to  
21   characterize the thermodynamic, cloud, and wind fields over West Africa (Thorncroft and  
22   Haile, 1995), and to relate them to precipitation anomalies.

23

1 The sparse amount of data available from West Africa has often proved a significant  
2 limitation in past studies. Cloudiness is often characterized using its infrared cloud top  
3 temperature or visible detection, which limits the resolution of underlying clouds.  
4 Radiosonde profiles are relatively infrequent in the region. Past studies have made  
5 significant strides, but there is still considerable uncertainty as to the details of cloud  
6 cover and precipitation, and its relationship with the thermodynamic structure over West  
7 Africa.

8

9 The purpose of this paper is to present a detailed assay of cloud and thermodynamic  
10 structure over a portion of West Africa not previously sampled with this rigor, and the  
11 monsoon season (May through September) is studied with particular emphasis. The data  
12 were collected using the United States Department of Energy's Atmospheric Radiation  
13 Measurement (ARM) Mobile Facility (AMF), which is a portable atmospheric laboratory.  
14 It is equipped with a suite of instruments designed to collect vertically-resolved  
15 measurements of the structure of the troposphere in cloudy and clear atmospheres in  
16 under-sampled regions. From January 2006 to January 2007, the AMF completed a year-  
17 long international deployment in Niamey, Niger, West Africa, at the Niger  
18 Meteorological Office at Niamey International Airport (N13° 28.638', E2° 10.547', 205  
19 m). Niamey is one of the warmest locations on Earth and it lies along one of the largest  
20 moisture gradients.

21

22 The AMF deployment (Miller and Slingo, 2007) was timed to coincide with the field  
23 phases and Special Observing Periods of the African Monsoon Multidisciplinary Analysis

1 (AMMA; Lebel et al., 2003) and the Geostationary Earth Radiation Budget (GERB;  
2 Harries et al., 2005) experiment. ARM participated in this international effort as part of  
3 the the Radiative Divergence using AMF, GERB and AMMA Stations (RADAGAST)  
4 field campaign. The primary purpose of the RADAGAST AMF deployment was to  
5 provide continuous measurements of the broadband upward and downward solar and  
6 thermal broadband radiative fluxes at the surface that could be combined with the  
7 corresponding measurements from GERB to estimate the radiative divergence across the  
8 atmosphere (Slingo et al., 2006; Miller and Slingo, 2007).

9

10 The AMF sampled a variety of conditions during its deployment and captured the annual  
11 and diurnal cycles of precipitation and cloudiness in the atmospheric column above  
12 Niamey. Time series and statistical analyses of these data are used in the sections that  
13 follow to examine the vertical structure of clouds and the connections between the  
14 thermodynamic profile and precipitation.

15

## 16 **2. METHODOLOGY**

17

18 The general approach taken here is to analyze the vertical profile of cloudiness in the  
19 column above Niamey using surface-based remote sensors and the accompanying  
20 thermodynamic environment using an assimilation procedure. The assimilated product  
21 based upon radiosonde ascents every three hours from Niamey International Airport  
22 complemented by a regional diagnosis of the thermodynamic state from a model. This  
23 approach enables specific features within the vertical profile of cloud structure to be  
24 related to specific thermodynamic features.

1

2 The AMF baseline suite of instruments used in this study include a 94-GHz (W-band)  
3 ARM cloud radar (WACR, Mead and Widener, 2005), a two-channel Microwave  
4 Radiometer (MWR), a twelve-channel Microwave Radiometer Profiler (MWRP), a  
5 micro-pulse lidar (MPL), a ceilometer, and surface meteorology. Observations from the  
6 WACR are available after mid-April 2006 due to late arrival of the newly fabricated  
7 cloud radar relative to the other AMF instrumentation. Continuous observations with the  
8 WACR were collected until the end of the deployment (end of 2006).

9

10 WACR Doppler moments and linear depolarization ratios (LDRs) were combined with  
11 MPL backscatter measurements and ceilometer cloud base heights to provide a cloud and  
12 precipitation mask and cloud boundaries with a temporal resolution of 5 sec and vertical  
13 resolution of 45 m. The basic approach adopted for this instrument synthesis is similar to  
14 that used in ARM's Active Remote Sensing of CLOUDS (ARSCL, Clothiaux et al., 2000)  
15 instrument merging product, which is based on 35-GHz Millimeter Cloud Radar  
16 observations rather than the 94-GHz WACR frequency. First, an MPL-based cloud mask  
17 is developed by comparing lidar backscatter measurements with returns during known  
18 clear sky periods. The MPL cloud mask is combined with ceilometer cloud base  
19 measurements to produce a best-estimate cloud base for each time period. Next, a  
20 WACR hydrometeor mask (cloud and precipitation) is derived based on signal-to-noise-  
21 ratio thresholds, which are determined for each time profile. The MPL and WACR cloud  
22 masks are then merged to take advantage of each instrument's strengths. For example,  
23 the radar signal is able to detect cloud tops, penetrating thick cloud layers that attenuate

1 the MPL signal, while the MPL is sensitive to very thin cloud layers that allude WACR  
2 detection.

3

4 Additional filtering of the merged WACR / MPL cloud mask is applied in the lower  
5 troposphere (below approximately 3.5 km) to flag probable insect returns. The Linear  
6 Depolarization Ratio (LDR) is used as the primary insect filter criterion because  
7 depolarization of a polarized transmitted pulse occurs when the target has an irregular  
8 shape. Insects, typically non-spherical, produce LDR returns that are significantly larger  
9 than spherical cloud droplets. Boundary layer returns with relatively high LDR, but low  
10 reflectivity (hence not likely to be associated with large oblate precipitation targets, were  
11 flagged as insect-contaminated and removed from the hydrometeor mask.

12

13 The cloud and precipitation mask, the cloud layer boundaries time series, and the  
14 recorded surface rainfall rate at the AMF site are used as input to a cloud and  
15 precipitation classification scheme. This scheme generates hourly estimates of cloud  
16 fraction, cloud base height, and cloud thickness for various cloud types. Cirrus clouds are  
17 defined as clouds with bases above 7 km, middle clouds as those having bases between 3  
18 and 7 km, and boundary layer clouds as those having tops below 3 km.

19

20 The goal of the precipitation scheme is to determine the fraction of time during which  
21 there is liquid precipitation in the column whether it reaches the surface in measurable  
22 quantity or not. Precipitation reaching the surface is identified and flagged when the  
23 reflectivity is greater than 0 dBZ in the lowest two radar measurement heights or it is

1 detected by the tipping bucket rain gauge. Precipitation not reaching the surface (virga)  
2 is identified and flagged when there is a cloud base in the 0 to 200 m range coupled with  
3 a cloud top above 3 km and a reflectivity of  $-17$  dBZ or more within the lowest 5.5 km  
4 (Frisch et al., 1995). For comparison, the hourly fraction of measurable surface  
5 precipitation (rainfall  $> 0.245$  mmh<sup>-1</sup>, which is the measurement threshold) is estimated  
6 using a tipping bucket rain gauge.

7

8 The environmental thermodynamic profile is measured at three-hour intervals using  
9 Vaisala RS-92 radiosondes. To circumvent the scale discordance between variability in  
10 the cloud field, which typically occurs on a scale of less than one-half hour, a data  
11 assimilation technique was created to estimate the thermodynamic profile at times  
12 between radiosonde launches. Radiosonde data are assimilated with surface-based  
13 meteorology and model-produced profiles from the European Centre for Medium Range  
14 Weather Forecasting (ECMWF; Jensen and Troyan, 2006). The ECMWF fields are  
15 expected to contain information about structural changes between radiosonde ascents  
16 because it is initialized with spatial information from the surrounding radiosonde network  
17 in West Africa. To assimilate the two thermodynamic fields, a temporal weighting  
18 function is applied to the radiosonde profile that gives it 100% weighting to the sonde  
19 observations at the observation time and height with steadily declining weight during the  
20 hour and a half before and after the observation time. As a matter of general course, the  
21 column integrated water vapor in the merged product is adjusted to agree with that  
22 measured by the MWR.

23

### 1        3. RESULTS

2

3        The analysis below is comprised of two components: an analysis of the seasonal and  
4        monthly distribution of cloud cover and an analysis of this structure in the context of the  
5        local thermodynamic environment during the monsoon. In the latter analysis, efforts are  
6        made to determine the links between observed precipitation and the characteristics of the  
7        cloud and thermodynamic fields.

8

#### 9        a. Cloud and Precipitation Fraction

10

11        During the October to April period (dry season), the lower atmosphere in Niamey has  
12        little cloud cover and high concentrations of dust blown from the Sahara Desert and  
13        aerosol from local and regional biomass burning. From May to September (wet season),  
14        the onset and end of the precipitation cycle is observed as indicated by the extension of  
15        the 94-GHz radar echoes to the surface in association with falling precipitation (Fig. 2).  
16        The wet season is characterized by convection of varying depth and intensity ranging  
17        from large, organized mesoscale complexes that generate severe weather and heavy  
18        rainfall to weakly or non-precipitating cumulus. The convection during the wet season  
19        occurs on a regular basis often coming in periods of enhancement, hereafter termed bursts,  
20        which may last for several days. These bursts are indicated by vertical “streaks” that  
21        often have clear spots between.

22

1 The most frequently observed cloud type through the seasonal cycle is cirrus in the layer  
2 between approximately 10 and 15 km, which persists in both the dry and wet seasons. A  
3 strongly resilient cirrus layer is frequently observed over tropical oceans (Comstock et al.,  
4 2002) and may be a prominent component of the continental tropical environment over  
5 West Africa if this nearly year-long cloud radar data set is representative. The onset of  
6 the monsoon in Niamey is characterized by the passage of the intertropical convergence  
7 zone (ITCZ). The periods of deep, strong radar echoes in mid-May and August mark the  
8 passage of the ITCZ during the study period.

9

10 Cirrus daily observed cloud fraction is generally less than 10% (November-December) in  
11 the dry season and increases to nearly 20% during the apex of the wet season (July and  
12 August; Fig. 3). Boundary layer clouds that are reflective enough to be detected by the  
13 cloud radar are virtually non-existent during the dry season (monthly mean cloud fraction  
14 ~ 1-2%) and relatively infrequent during the wet season (monthly mean cloud fraction  
15 10% or less). This may be due to the relative dryness of air from the Sahara, which is  
16 often found above a shallow moist layer, as shown later. Relative to low and high clouds,  
17 mid-level cloudiness exhibits a strong seasonal cycle in monthly mean cloud fraction (1-  
18 5% in dry season, 20-25% in wet season). The seasonal fluctuation in mid-level  
19 cloudiness is due to the emergence of deep convection during the monsoon season and, as  
20 will be shown subsequently, a peak in mid-level cloudiness at the freezing level.

21

22 The deployment-average profile of cloud and precipitation fraction (Fig 3b) exhibits a  
23 bimodal structure with a maximum of 10% at 11.5 km (cirrus clouds) and a secondary

1 peak (7.5%) at 5.5 km, 1 – 1.5 km above the height of the melting layer in Niamey is  
2 indicated by the location of the radar bright band (not shown) during the wet season and  
3 by the thermodynamic profiles shown subsequently. The cirrus monthly mean cloud  
4 thickness is 1 km with a standard deviation from 600 m (dry season) to 1500 m (wet  
5 season). The monthly averaged cirrus cloud top height varied from 11.5 to 12.5 km (Fig.  
6 3), although the small depression in the cirrus cloud top height observed in August is  
7 attributed to WACR attenuation. The monthly average mid-level cloud top height is 6 km  
8 during the wet season and the monthly averaged cloud thickness is 1 km (Fig. 3).

9

10 During the wet season, precipitation was observed frequently, but several days with no  
11 precipitation were observed (Fig.2 and Fig.4). Typical precipitation events (Fig. 1) lasted  
12 for 2-6 hours. Convective precipitation cores with rainfall rates  $>10 \text{ mmh}^{-1}$  and trailing  
13 stratiform precipitation were often observed, while other times only trailing stratiform  
14 precipitation generated by middle and cirrus clouds was observed. The precipitation  
15 fraction, defined as the percentage of time during a given period in which precipitation  
16 was observed by the WACR, was as high as 20 - 40 % on individual days. The monthly-  
17 averaged precipitation fraction was lower (5-10%), with the maximum in August (Fig. 3).  
18 The daily-accumulated rainfall measured by the tipping bucket at the AMF site was  
19 highly variable. Overall, during the AMF deployment, there were 11 different days when  
20 10 mm or more of accumulated rainfall was measured; there were 19 days with  
21 accumulated rainfall amount between 2 – 10 mm and more than 30 days with  
22 accumulated rainfall amounts of less than 2 mm.

23

1 To determine the percentage of the observed precipitation that evaporated before  
 2 reaching the surface, the fraction of time the WACR detected precipitation at the surface  
 3 that was not measured (rainfall rate  $< 0.245 \text{ mmh}^{-1}$ ) by the tipping bucket was computed.  
 4 About 50% of the WACR precipitation detections at the surface (e.g., lowest altitude  
 5 radar range gate contains hydrometeor echo), are produced by rainfall rates below the  
 6 minimum detectable rain rate by the tipping bucket (Fig. 4). When the rainfall rate is  
 7 small and immeasurable by the tipping bucket rain gauge, a decrease of the radar  
 8 reflectivity with decreasing altitude is observed, signaling raindrop evaporation during  
 9 descent through the deep (4-4.5 km) and the extremely dry conditions that often exist  
 10 beneath the melting layer. It appears that much of the rainfall that evaporates before  
 11 reaching the surface is associated with the trailing stratiform regions.

12

### 13 b. Thermodynamic Environment

14

15 Convection is the primary source of rainfall and cloud cover during the rainy season in  
 16 West Africa. This convection is a consequence of the availability and realization of  
 17 Convective Available Potential Energy (CAPE). The CAPE for each half-hour profile is  
 18 computed using the  $\theta_e$  and  $\theta_{es}$  profiles using

19

$$20 \quad CAPE = \int_{LFC}^{EL} \frac{g(\theta_{e[\max]} - \theta_{es}(z))}{(1 + \gamma)\bar{\theta}} dz \quad (1)$$

21

1 where LFC is the Level of Free Convection, EL is the equilibrium level,  $g$  is gravity,  
2  $\theta_{e[\max]}$  is the maximum value of  $\theta_e$  in the column,  $\bar{\theta}$  is the mean potential temperature in  
3 the layer, and  $z$  is height. In (1),  $\gamma = L^2 q_s (c_p R_v T^2)^{-1}$ , where  $L$  is the latent heat of  
4 vaporization,  $q_s$  is the saturation specific humidity,  $c_p$  is the specific heat at constant  
5 pressure,  $R_v$  is the universal gas constant at constant volume, and  $T$  is temperature.

6

7 In each thermodynamic profile, the largest value of  $\theta_e$  in the column is taken as a  
8 reference point,  $\theta_{e[\max]}$ . This maximum is typically observed in the layer between the  
9 surface and 700-mb, which is, interestingly, near the top of the semi-permanent dust layer  
10 as measured using the MPL (not shown). Once this level is identified, the lowest value of  
11  $\theta_{es}$  in the layer above is located and recorded. If this value is not lower than the  
12 maximum  $\theta_e$ , no CAPE is present and the profile is flagged accordingly. Otherwise, the  
13 Level of Free Convection (LFC) is determined by locating the point on the  $\theta_{es}$  profile  
14 above the  $\theta_e$  maximum in which the values of the  $\theta_e$  maximum and value  $\theta_{es}$  are  
15 equivalent; this point is the bottom boundary of the CAPE integral (1). The top boundary  
16 is the point at which the maximum value of  $\theta_e$  and  $\theta_{es}$  are once again equal, which is  
17 defined as the Equilibrium Level (EL). This method was selected because the complexity  
18 of the thermodynamic profiles made other approaches difficult to automate. This  
19 technique does have drawbacks in that it often overestimates the amount of CAPE  
20 (Emanuel, 1994), so vertical velocity estimates are also prone to overestimation and are  
21 avoided in this study. Despite its inclination to overestimate the actual magnitude of the  
22 CAPE, it is quite capable of portraying changes in CAPE.

23

1 To illustrate some typical features of the thermodynamic and cloud structure for a typical  
2 convective event in the region, we selected a storm complex observed on 9 June 2006 for  
3 further investigation. During this event, convective rainfall commenced around 0700  
4 UTC and ended around 1200 UTC, and prior to the event, there were no clouds detected  
5 for a period of hours. The pre-storm and post-storm environments (Fig. 5a-b) for this  
6 convective event show a considerable change in CAPE, represented by the positive area  
7 in the sounding in the pre-storm environment and virtually no CAPE in the post-storm  
8 profile. The CAPE in the pre-storm environment exists for parcels above approximately  
9 900 mb, but is the largest and easiest to realize for parcels in the region around 700 mb.

10

11 The profile of  $\theta_e$  in the pre-storm environment shows significant layering and no well-  
12 mixed regions, which would have a constant value of  $\theta_e$  as a function of pressure. This  
13 layering is indicative of a lack of convective overturning in the column prior to the onset  
14 of the convection. The pre-storm profile of  $\theta$  (Fig. 5c) shows highly stable regions from  
15 the surface to 800 mb and above 400 mb with a less stable region between. After the  
16 storm passes, the  $\theta_e$  profile shows considerably less layering and is nearly well-mixed  
17 (Fig. 5b) in a region that is just above the layer that was previously less stable between  
18 800 and 400 mb. Moisture was transported higher in the atmosphere as evidenced by the  
19 pre- and post storm specific humidity profiles (Fig. 5d), while the relative humidity and  
20 cloudiness increased above 500-mb. A rapid return to an environment that contained  
21 significant CAPE was observed within a few hours after the end of the rainfall associated  
22 with this event.

23

1 An interesting characteristic of the convective environment observed at Niamey is that a  
2 maximum in  $\theta_e$  is frequently observed in the vicinity of 700-mb accompanied by a  
3 minimum in  $\theta_{es}$  in the mid- and upper troposphere. There is almost always considerable  
4 layering in the profile as would be expected if the air masses in different regions of the  
5 column had different points of origin and had been subjected to a range of different  
6 processes. Such structure is not atypical in environments that frequently experience  
7 strong convection, but the notable absence of well-mixed layers in most of the profiles is  
8 indicative of significant convective inhibition.

9

10 To examine the evolution of the cloud, thermodynamic, and precipitation structure  
11 through the rainy season, a time series of key variables was constructed. Estimated  
12 thermodynamic profiles were available at one-minute intervals and cloud profiles at sub-  
13 one-minute intervals. A half-hour averaging period was selected for the cloud profiles  
14 because experience has shown that the radiative impacts of the cloud field involve  
15 hemispheric contributions despite the narrow beam cloud measurements available from  
16 the WACR. There is no guarantee that these averages capture the hemispheric variability  
17 in the vicinity of Niamey, but they are superior to single samples or significantly longer  
18 averaging periods that significantly smear details. The thermodynamic profile at the  
19 center time of each half-hour bin was recorded and interpolated to be consistent with the  
20 height-resolution of the WACR.

21

22 The running-mean value of the time series of CAPE for the period encompassing the  
23 summer monsoon shows that CAPE is first observed in early May and quickly ramps to a

1 value of approximately  $5000 \text{ J kg}^{-1}$  where it remains for the duration of the convective  
2 season (Fig. 6a). While the running-mean CAPE rarely exceeds  $5000 \text{ J kg}^{-1}$ , the  
3 instantaneous values can be much larger on occasion. Viewing the rainy season as a  
4 whole, CAPE remains relatively constant and does not appear to steadily increase with  
5 time as the monsoon evolves. There are also periods in which CAPE is quite large for a  
6 long period, but little or no precipitation is observed. Clearly, the relationship between  
7 CAPE and precipitation is tenuous during the rainy season of 2006.

8

9 The soundings collected in Niamey were almost always conditionally unstable. Thus, the  
10 Lifting Condensation Level (LCL) is a critical point in the column because saturation is  
11 required to realize the instability. The profile of the LCL for each half-hour profile was  
12 computed and the lowest value of the LCL above ground level was recorded (Fig 6b).  
13 Each point in the column possesses a unique LCL and, theoretically, the parcel requiring  
14 the least amount of lifting should be the initiation point of convection if the entire column  
15 is lifted by an equal increment. That said, the initial convection will induce further lifting  
16 in the layers below the initiation point and eventually the parcel with the LCL closest to  
17 the surface will become the cloud base. The LCL steadily declines from a level above 4-  
18 km in April to less than 0.5 km in the July through October period. A strong relationship  
19 between the LCL and accumulated precipitation is suggested and relationships between  
20 cloud cover, the LCL, and precipitation will be examined shortly.

21

22 Details of the mixing processes that accompany convective overturning and the state of  
23 the vertical gradients in the lower atmosphere are revealed by analyzing fluctuations half-

1 hour in  $\theta_e$  and  $\theta_{es}$  at a specific level or at the surface (Fig 6c). These short-term  
2 fluctuations are generally a consequence of vertical mixing processes, whereas longer  
3 term changes are ascribable to advection and radiation. Half-hour fluctuations in surface  
4  $\theta_e$  (and  $\theta_{es}$ ) were computed by subtracting the maximum and minimum values for each  
5 half-hour period.

6

7 Coincident with the onset of the monsoon is a rapid increase in the half-hour fluctuations  
8 in  $\theta_e$ , which are a consequence in changes in both moisture and temperature. This  
9 increase is indicative of mixing processes operating upon the increased vertical gradient  
10 in  $\theta_e$  that is associated with the arrival of a cooler and moister air mass near the surface  
11 associated with the monsoon. Unlike the fluctuations in  $\theta_e$ , which seem to ramp to a  
12 relatively constant value at the beginning onset of the monsoon, fluctuations in  $\theta_{es}$ , which  
13 are driven entirely by the vertical temperature gradient, show a steady decrease  
14 associated with a steady reduction in the vertical temperature gradient as the monsoon  
15 proceeds. Thus, the increased fluctuations in  $\theta_e$  at the onset of the monsoon appear to be  
16 associated with a substantial increase in the vertical moisture gradient, rather than a  
17 temperature gradient. The strong correlation between a steady reduction of the  
18 fluctuations in  $\theta_{es}$ , which are associated with a reduction in the vertical temperature  
19 gradient, and the onset of precipitation suggests that the vertical temperature gradient  
20 (stability) plays a critical role in convective development, as expected.

21

22 A monthly climatology of the cloud coverage and thermodynamic profiles was  
23 constructed to demonstrate the evolution during the rainy season. A one-month time

1 window was selected because longer term averages tend to smear details due to the  
2 migration of the ITCZ.

3

4 The monthly averages of the cloud coverage profile (Fig. 7) show the evolution of the  
5 cloud field from the onset through the end of the rainy season (May through October).

6 The cloud coverage is characterized by recording the monthly mean as well as the  
7 maxima and minima in the half-hour averaged cloud coverage at each height during the  
8 month. The latter variable reveals layers that experienced no periods of complete  
9 overcast during the month. Separate peaks in the cloud fractional coverage and relative  
10 humidity are discernable in the lower and upper troposphere during May (Fig. 7a) and  
11 there is a layer above 6-km that was not completely overcast at any time during this  
12 month (not shown). This lack of overcast implies that there were no convective events  
13 lasting more than one-half hour that filled the entire depth of the troposphere. In May, no  
14 appreciable precipitation was observed and the LCL is, on the average, just below 3-km.

15

16 The ITCZ passes Niamey at the end of May as it migrates to the north. Separate peaks in  
17 the cloud fractional coverage in the vicinity of 5-6 km and above 10-km are still  
18 discernable in June, but less discernable in July through September. The peaks appear  
19 again with high fidelity at the conclusion of the monsoon in October (and November,  
20 which is not shown). The mean accumulated precipitation and precipitation rate are the  
21 largest in August, but are significant during the period of June through September, as  
22 previously noted. The LCL moves steadily closer to the surface as the summer  
23 progresses and appears to modulate the mean monthly storm accumulation and peak

1 rainfall, as previously noted. The LFC also moves closer to the LCL, which increases the  
2 ease with which convection may realize the conditional instability that is present. The  
3 extremes in the relative humidity profile reveal that the variability in low-level relative  
4 humidity is significantly reduced at the height of the monsoon. Cloudiness that extends  
5 through the entire depth of the troposphere is observed throughout the monsoon season as  
6 indicated by the cloud frequency profiles; each layer experiences at least one half-hour  
7 period with complete overcast during this period (not shown). Despite this apparently  
8 cloudy environment, cloud fractional coverage remains modest in each individual layer  
9 (around 10% at the height of the monsoon).

10

11 Unlike the LCL, which appears highly correlated with precipitation, the monthly-mean  
12 CAPE shows only minor variation from May through October, as suggested in the time  
13 series analyzed previously. This suggests that there is significant CAPE most of the time,  
14 a thought that is reinforced by the rapid recovery of the atmosphere after the convective  
15 event on 9 June (Fig. 5). Despite a noticeable increase in the relative humidity in the  
16 lowest levels of the troposphere, the temperature difference between  $\theta_e$  and  $\theta_{es}$  in the  
17 profiles remains relatively constant from month to month as does the difference in  
18 temperature between the maximum  $\theta_e$  in the profile and the minimum  $\theta_{es}$  above, which is  
19 related to the amount of CAPE.

20

21 The association between cloud coverage and the freezing level has been documented in  
22 tropical regions (Mather et al. 1998; Johnson et al. 1999) and the monthly profiles from  
23 Niamey are no exception. There is a maximum at or just above the zero degree isotherm

1 in the monthly profiles of cloud frequency in each of the seven months examined in this  
2 study. The thermodynamic profiles also show a clear pivot at the freezing level. The  
3 minimum observed  $\theta_e$  in the monthly mean also shows a sharp minimum at the freezing  
4 level.

5  
6 Withdraw of the monsoon layer raises the LCL and is associated with increasing  
7 intrusions of dry air at mid-levels (Namguti et al. 1995, Yoneyama and Parsons 1999) as  
8 evidenced by a noticeable minimum in the mean relative humidity in October and  
9 November (not shown). These features conspire to attenuate convection (Brown and  
10 Zhang 1997, Johnson et al. 1999, Redelsperger et al. 2002, Jensen and Del Genio 2006),  
11 which leads to the discrimination of separate peaks in the cloud coverage frequency  
12 profiles in the lower and upper troposphere. By November, extreme drying in the lower  
13 half of the column associated with injections of the Saharan air layer is apparent, and  
14 accordingly, CAPE is diminished and precipitation ceases.

15  
16 The sensitivity of the Sahel and West Africa to precipitation is well known and these data  
17 demonstrate some important functional relationships (Fig. 8). Correlations between the  
18 monthly mean rainfall accumulation during each half-hour period and the monthly mean  
19 CAPE ( $R^2=0.04$ ) reinforce the lack of any relationship between precipitation (amount or  
20 rate) and the relative quantity of available CAPE (Fig. 8a). The month of November was  
21 excluded in the above analysis because there was no CAPE or precipitation, which  
22 illustrates the necessity of CAPE in the precipitation process despite the lack of any  
23 relationship between the quantity of CAPE and the quantity of precipitation. Conversely,

1 a high correlation ( $R^2=0.74$ ) exists between the monthly mean rainfall and the height of  
2 the LCL, excluding November (Fig. 8b). If November, which is in the dry season, is  
3 included, this correlation is diminished ( $R^2=0.62$ , not shown) slightly.

4

5 An elevated level of cloudiness frequency through the depth of the troposphere is a good  
6 indicator of convective activity, so the sum of the mean fractional cloudiness over all 265  
7 20-m deep layers is used as a cloudiness index for the purpose of testing the relationships  
8 between cloud cover, precipitation, LCL height, and the height of the zero-degree  
9 isotherm (Fig. 8c-f). The monthly mean LCL is strongly correlated with an elevated  
10 value of the cloudiness index ( $R^2=0.81$ ; Fig. 8c), which is in turn strongly correlated with  
11 the monthly mean accumulated precipitation ( $R^2=0.89$ ; Fig. 8d) and the monthly mean  
12 precipitation rate ( $R^2=0.96$ ; Fig. 8f). Strong correlations between the latter two variables  
13 and cloud cover are somewhat expected, though the strong correlations provide  
14 reassurance as to the self-consistency of the data set.

15

#### 16 **4. SUMMARY AND DISCUSSION**

17

18 Combining the WACR, MPL, ceilometers, radiosonde, and surface meteorological  
19 observations we develop vertically-resolved cloud statistics for the one-year-long Niamey,  
20 Niger deployment of the AMF and analyze them in the context of the thermodynamic  
21 environment and precipitation. The analysis spans the dry and wet (monsoon) seasons.  
22 The dry season (October to April) is characterized by persistent tropical cirrus of  
23 approximately 20% average coverage and 1-km thickness. This cirrus is characterized by

1 bursts that in the form of peaks in the cloud frequency, which lasted on the order of a few  
2 days, surrounded by periods with little or no cirrus. Frequent dust outbreaks were  
3 observed during the dry season and boundary layer and middle layer clouds are rarely  
4 observed. The dryness of the Saharan air masses in the lower levels is the likely cause of  
5 attenuated boundary layer cloudiness. The wet season (May to September) is  
6 characterized by intermittent convection of varying intensity that produced several hours  
7 of precipitation on some days and other days with no precipitation. Intense rainfall  
8 events accounted for most of the accumulated surface precipitation, although the most  
9 frequently observed precipitation events produced rainfall that evaporated before it  
10 reached the surface.

11

12 It is difficult to usefully compare observations from a single point with regional  
13 composite structures computed by models, so we do so with some trepidation and only in  
14 generalities. The surface values of  $\theta_e$  appear roughly consistent with those in Hodges  
15 and Thorncroft (1997), which are derived from ECMWF data, though the large vertical  
16 gradient and sharp peak in  $\theta_e$  observed in the present study during the rainy season is not  
17 well represented. The location of this maximum in  $\theta_e$  is often coincident with the top of  
18 the dust layer, as measured with the MPL, so we conjecture that its occurrence at this  
19 level could be related to radiative processes associated with the thick dust and aerosol  
20 layer. We also observed a minimum in  $\theta_{es}$  in the mid-levels that appear inconsistent with  
21 the ECMWF rainy season cross-sections. While these are noteworthy observations, a  
22 more appropriate comparison would utilize regional radiosonde data, which is beyond the  
23 scope of this study.

1

2 The rainy season is predicated upon the continuous availability of CAPE. The values of  
3 CAPE that we estimate ( $\sim 5000 \text{ J kg}^{-1}$ ) are substantially larger than those found by  
4 Monkram (2002;  $2000 \text{ J kg}^{-1}$ ), most likely because (1) our method tends to exaggerate the  
5 absolute amount of CAPE because we determine its value from the parcel with the  
6 maximum positive area, (2) we use a conservative variable approach equivalent potential  
7 temperatures, and (3) the data set analyzed by Monkram (2002) uses only low resolution  
8 data from mandatory levels, which may underestimate the maximum CAPE given the  
9 sharp vertical gradients that are observed in our data. The true mean value of CAPE in  
10 this region probably lies between these two extremes.

11

12 Despite the availability of this CAPE to fuel convection, no substantial relationship  
13 between the amount of CAPE, cloudiness, and precipitation exists in these data. This is  
14 consistent with Sherwood (1999) who showed that although there is a minimum amount  
15 of CAPE necessary for convection to occur in the Tropics, increased CAPE does not  
16 necessarily result in more vigorous convection. Jensen and Del Genio (2006) also show  
17 only a weak correlation between the magnitude of CAPE and convective cloud top  
18 heights in the Tropical Western Pacific. Our results show lower correlation between  
19 CAPE and precipitation than found by Monkram (2002), though both studies show  
20 relatively weak relationships between the two variables.

21

22 The occurrence of deep convection and its accompanying rainfall is best correlated with a  
23 reduction in the height of the LCL and an accompanying reduction in the height of the

1 LFC, which enhances the probability of cloud development in the observed conditionally  
2 unstable environment. Lowering of the LFC also changes the distribution of positive area  
3 in a manner that provides more buoyancy at lower levels. Changes in the structure of the  
4 temperature profile in the lower troposphere correspond with the occurrence of  
5 convection and precipitation. The observed decrease in the LCL and LFC are, to a large  
6 extent, modulated by cooling of the lower troposphere while the integrated amount of  
7 moisture remains relatively constant.

8

9 The discordance in the time series of  $\theta_e$  and that of  $\theta_{es}$ , suggests that a steady reduction in  
10 the vertical temperature gradient in the lower troposphere is primarily responsible for the  
11 observed decrease in the LCL and the realization of CAPE. At the height of the monsoon,  
12 the  $\theta_e$  and  $\theta_{es}$  fluctuations are roughly equal. One explanation for this agreement is that  
13 temperature profile is modulating the profile of  $\theta_e$ , while the moisture profile remains  
14 relatively constant. Examination of the soundings suggests that the approximately 50°K  
15 fluctuations in  $\theta_e$  are a result of mixing through the layer between the surface and 700 mb.  
16 This is approximately the level of maximum  $\theta_e$  in the column, so the convection is  
17 serving to reduce the vertical gradients in the lower troposphere as expected.

18

19 A salient aspect of many of the thermodynamic profiles and accompanying cloud  
20 structure examined is significant layering. The lower 300 mb of the troposphere was, by  
21 and large, more stable than the mid-layers. Well-mixed layers are rarely observed.  
22 While the causes of this layering probably involve a complex variety of processes, it  
23 contributes significantly to the observed cloud and thermodynamic structure.

1

2 Like many tropical regions, the zero-degree isotherm is intimately related to the vertical  
3 structure of cloudiness and to structural changes in the thermodynamic profile itself. A  
4 maximum in cloudiness is always observed at or just above the zero degree isotherm and  
5 monthly mean values of  $\theta_e$  and  $\theta_{es}$  show a sharp minimum at this level. A particularly  
6 interesting association between the maximum observed  $\theta_e$  during each month and the  
7 zero degree isotherm is present in these data. The causes of these significant changes in  
8 the vertical structure of the column are apparently related to the change in phase of  
9 precipitation. There are several potential explanations for the observed sensitivity of the  
10 tropical atmosphere to the location of the zero-degree isotherm. One explanation is that  
11 the temperature of the condensate must remain constant through the depth of its change  
12 of phase. This cold condensate is falling into a warmer and moister layer and it may  
13 physically cool the layer. This would result in the observed increase in relative humidity,  
14 decrease in temperature, and increase in cloudiness due to additional cooling of nearly  
15 saturated moist air. Another explanation is that newly glaciated particles are detrained  
16 from the main body of the cloud due to aerodynamics and advected laterally where they  
17 are subsequently evaporated. Whatever the combination of processes that produces the  
18 observed minima at the freezing level, it is clear that condensate freezing and melting is  
19 substantially correlated with the thermodynamic profile in West Africa.

20

21 The omnipresence of CAPE during the rainy season and the relationship between rainfall  
22 occurrence and the height of the LCL exposes some potential local mechanisms that  
23 could alter the occurrence of rainfall in the region. Mechanisms that cool or further

1   moisten the lowest levels of the troposphere could impact the precipitation process,  
2   assuming that the data set considered here is representative.

3

#### 4       **5. ACKNOWLEDGEMENTS**

5

6   Many dedicated professionals have contributed to the design, construction, and  
7   deployment of the ARM Mobile Facility. Mike Alsop, Betsy Andrews, Mary Jane  
8   Bartholomew, Dick Egan, Larry Jones, Kim Nitschke, John Ogren, Rex Peterson, Doug  
9   Sisterson, Jimmy Voyles, and Kevin Widener have made notable contributions.

10

#### 11       **6. REFERENCES**

12

13   Brown, R. G. and C. Zhang, 1997: Variability of mid-tropospheric moisture and its effect  
14   on cloud-top height distribution during TOGA-COARE. *J. Atmos. Sci.*, **54**, 2760-2774.

15

16   Burpee, R., 1972: The origin and structure of easterly waves in the lower troposphere of  
17   North Africa, **29**, 77-90.

18

19   Charney, J.G., 1975: Dynamics of deserts and droughts in the Sahel, *Quart. J. Roy.*  
20   *Meteor. Soc.*, **101**, 193-202.

21

22   Clothiaux, E. E., G. G. Mace, T. P. Ackerman, T. J. Kane, J. D. Spinhrine, and V. S.  
23   Scott, 1998: An automated algorithm for detection of hydrometeor returns in micro pulse

1 lidar data. *J. Atmos. And Oceanic Technol.*, **15**, 1035-1042

2

3 Clothiaux, E. E., Thomas P. Ackerman, Gerald G. Mace, Kenneth P. Moran, Roger T.  
4 Marchand, Mark A. Miller, Brooks E. Martner, 2000: Objective Determination of Cloud  
5 Heights and Radar Reflectivities Using a Combination of Active Remote Sensors at the  
6 ARM CART Sites. *J. Appl. Meteor.*, **39**, 645-665.

7

8 Comstock, J. M. , T. P. Ackerman and G. G. Mace, 2002: Ground-based lidar and radar  
9 remote sensing of tropical cirrus cloud at Nauru Island: Cloud statistics and radiative  
10 impacts. *J. Geophys. Res.*, **107**. No. D23, 4714, doi:10.1029/2002JD002203.

11

12 Cook, K.H., 1999: Generation of the African easterly jet and its role in determining West  
13 African precipitation, **12**, 1165-1184.

14

15 Desbois, M., T. Kayiranga, B. Gnamien, S. Guessous, and L. Picton, 1988:  
16 Characterization of some elements of the Sahelian climate and their interannual  
17 variations for July 1983, 1984, and 1985 from the analysis of METEOSAT ISCCP data, *J.*  
18 *Climate*, **1**, 867-904.

19

20

21 Emanuel, K.A., 1994: *Atmospheric Convection*, Oxford University Press, pp. 580.

22

1 Frisch, A. S., C. W. Fairall, and J. B. Snider, 1995: Measurement of stratus cloud and  
2 drizzle parameters in ASTEX with a K<sub>a</sub>-band Doppler radar and a microwave radiometer.

3 *J. Atmos. Sci.*, **52**, 2788–2799

4

5 Harries, J. E. and coauthors, 2005: The Geostationary Earth Radiation Budget (GERB)  
6 Experiment. *Bull. Amer. Meteorol. Soc.*, **86**, 945-960.

7

8 Hodges, K.I., and C.D. Thorncroft, 1997: Distribution and statistics of African mesoscale  
9 convective weather systems based on the ISCCP Meteosat imagery, *Mon. Wea. Rev.*, **125**,  
10 2821-2837.

11

12 Hoerling, M., J. Hurrell, J. Eischeid, and A. Phillips, 2006: Detection and Attribution of  
13 Twentieth-Century Northern and Southern African Rainfall Change. *J. Climate*, **19**, 3989-  
14 4008

15

16 Jensen, M.P. and A.D. Del Genio, 2006: Factors limiting convective cloud top height at  
17 the ARM Nauru Island climate research facility. *J. Climate*, **19**, 2105-2117.

18

19 Jensen, M. P. and D. Troyan, 2006: Continuous water vapor profiles for the fixed  
20 atmospheric radiation measurement sites: 2006 ARM Metric first quarter report. U.S.  
21 Department of Energy. DOE/SC-ARM/P-06-002.

22

- 1 Johnson, R. H., T. M. Rickenbach, S. A. Rutledge, P. E. Ciesielki, and W. H. Shubert,  
2 1999: Trimodal characteristics of tropical convection. *J. Climate*, **12**, 2397-2418.  
3
- 4 Kollias, P., B.A. Albrecht, and F. D. Marks, Jr., 2002: Why Mie? Accurate observations  
5 of vertical air velocities and rain drops using a cloud radar. *Bull. Amer. Met. Soc.*, **83**,  
6 1471-1483.  
7
- 8 Laing, A.G. and J.M. Frisch, 1993: Mesoscale convective complexes in Africa, **121**,  
9 2254-2263.  
10
- 11 Lamb, P.J., 1978: Case studies of Tropical Atlantic surface circulation patterns during  
12 recent Sub-Saharan weather anomalies: 1967 and 1968, **106**, 482-491.  
13
- 14 Lebel, T., Redelsperger, J.-L., and Thorncroft, C., 2003: African Monsoon  
15 Multidisciplinary Analysis (AMMA) Project. *GEWEX News*, **13**, No. 4, 8-9, November  
16 2003.  
17
- 18 Mather, J. H., M. P. Jensen and T. P. Ackerman, 1998: Characteristics of the  
19 atmospheric state and the surface radiation budget at the Tropical Western  
20 Pacific ARM site. *Geophys. Res. Lett.*, **25**, 4513-4516.  
21
- 22 Mead J. B. and K. Widener, 2005: W-band ARM Cloud Radar. Preprints, *32th Int. Conf.*  
23 *on Radar Meteorology*, Amer. Meteor. Soc., Albuquerque, NM.

1

2 Miller, M.A. and A. Slingo, 2007: The Atmospheric Radiation Measurement (ARM)  
3 Mobile Facility (AMF) and its first international deployment: measuring radiative flux  
4 divergence in West Africa, *Bulletin of the American Meteorological Society*, **88**, 1229-  
5 1244.

6

7 Monkam, D., 2002: Convective available potential energy (CAPE) in northern Africa and  
8 tropical Atlantic and study of its connections with rainfall in central and west Africa  
9 during summer 1985, *Atmos. Res.*, **62**, 125-147.

10

11 Namaguti, A., R. Oki, K. Nakamura, K. Tsuboki, N. Misawa, T. Asai, and Y. -M.  
12 Kodma, 1995: 45-day-period variation and low-level dry air observed in the equatorial  
13 western Pacific during TOGA COARE. *J. Meteor. Soc. Japan*, **73**, 267-290.

14 Otterman, J., 1974: Baring high-albedo soils by overgrazing: A hypothesized  
15 desertification mechanism, *Science*, **186**, 531-533.

16

17 Redelsperger, J. -L., D. B. Parsons and F. Guichard, 2002: Recovery processes and  
18 factors limiting cloud-top height following the arrival of a dry intrusion observed during  
19 TOGA COARE. *J. Atmos. Sci.*, **59**, 2438-2457.

20

21 Sherwood, S. C., 1999: Convective precursors and predictability in the tropical Western  
22 Pacific. *Mon. Wea. Rev.*, **127**, 2977-2991.

23

1 Slingo, A., T.P. Ackerman, R.P. Allan, E.I. Kassianov, S.A. McFarlane, G.J. Robinson,  
2 J.C. Barnard, M.A. Miller, J.E. Harries, J.E. Russell , S. Dewitte, 2006: Observations of  
3 the impact of a major Saharan dust storm on the Earth's radiation budget. *Geophys. Res.*  
4 *Lett.*, **33**, L24817, doi:10.1029/2006GL027869.

5

6 Thorncroft, C.D., and M. Haile, 1995: The mean dynamic and thermodynamic fields for  
7 July 1989 over tropical north Africa and their relationship to convective activity. *Mon.*  
8 *Wea. Rev.*, **123**, 3016-3031.

9

10 Tselioudis, G. and P. Kollias, 2007: Evaluation of ECMWF cloud type simulations at the  
11 ARM Southern Great Plains site using a new cloud type climatology, *Geophys. Res. Lett.*,  
12 **35**: Art. No. L03803.

13

14 Yoneyama, K. and D. B. Parsons, 1999: A proposed mechanism for the intrusion of dry  
15 air into the Tropical Western Pacific region. *J. Atmos. Sci.*, **56**, 1524 – 1546.

16

17

18

## 1 7. FIGURE CAPTIONS

2

3 Fig. 1: Example of 94-GHz cloud radar reflectivity on August 8, 2006 at Niamey, Niger  
4 during the AMF deployment. The black line indicates the tipping bucket surface rainfall  
5 rate in  $\text{mmh}^{-1}$

6

7 Fig. 2: Daily observed cloud fraction in Niamey during the AMF deployment. The cloud  
8 fraction is derived from measurements from the 94-GHz radar, the micro-pulse lidar and  
9 the ceilometer. The vertical resolution is 260 m and a 5-day temporal average is applied  
10 to the daily cloud fraction profiles.

11

12 Fig. 3: (a) Monthly-averaged cloud and precipitation fraction. The monthly mean and  
13 standard deviation of cirrus cloud top (white line), middle clouds tops (white line), cirrus  
14 cloud thickness (yellow line) and middle clouds thickness (red) are also shown. (b) The  
15 deployment-mean cloud and precipitation fraction during the AMF deployment at  
16 Niamey, Niger.

17

18 Fig. 4 Daily- and monthly-observed fractional coverage of precipitation (radar echo)  
19 (blue thin and thick lines), accumulated daily rainfall (in mm, black squares) and daily-  
20 and monthly-observed fractional coverage of measurable precipitation by the tipping  
21 bucket (red thin and thick lines, rainfall  $> 0.245 \text{ mmh}^{-1}$ ) at the AMF site.

22

1 Figure 5. Pre- (0500 UTC) and post-storm (1300 UTC) environments for 9 June 2006.  
2 (a) The equivalent potential (red) and saturation equivalent potential temperatures (green)  
3 for the pre-storm environment. The Level of Free Convection (LFC) and Equilibrium  
4 Level (EL) are indicated and the blue asterisk and black square represent reference  
5 thermodynamic levels referred to in the text. The region bounded by the dashed black  
6 line and the green line is the positive area. (b) as in (a), but for the post-storm  
7 environment. The dashed green line is the saturation equivalent temperature from the  
8 pre-storm environment for reference. (c) The potential temperature profile for the pre-  
9 (solid) and post-storm environments. (d) The mixing ratio (red) and the relative humidity  
10 (blue) for the pre-(solid) and post-storm (dashed) environments. The black line with  
11 filled-circles is the non-zero percent coverage of clouds in the post-storm environment.

12

13 Figure 6. (a) The temporal relationship between CAPE and precipitation. The yellow line  
14 connects the half-hour estimations of CAPE and the blue line is a running mean through  
15 the raw CAPE estimates. The red lines are half-hour values of accumulated precipitation  
16 multiplied by  $1.0 \times 10^4$  for display convenience. (b) The half-hour average LCL (blue)  
17 versus accumulated precipitation (red). (c) Half-hour fluctuations in  $\theta_e$  and  $\theta_{es}$  versus  
18 accumulated precipitation multiplied by 100 for display convenience. (d) Half-hour  
19 accumulated precipitation and precipitation rate versus half-hour fluctuations in  $\theta_e$ .

20

21 Figure 7. (left column) Monthly mean profiles of cloud fractional coverage (green),  
22 relative humidity (black), minimum relative humidity and maximum relative humidity  
23 envelope (black dashed left and right of solid black line) for the months of May through

1 October (a-f). The monthly mean accumulation from individual precipitation events is  
2 indicated with the filled red circle on the height axis and the monthly mean precipitation  
3 rate from individual precipitation events is indicated with the inverted green triangle.  
4 (right column) Monthly mean profiles of  $\theta$  (black),  $\theta_e$  (red),  $\theta_{es}$  (green), and minimum  $\theta_e$   
5 (black dashed) and the monthly mean CAPE/1000 ( $\text{J kg}^{-1}$ ). (left and right columns) The  
6 blue dashed line on each plot is the mean monthly level of the zero-degree isotherm and  
7 the black dot-dashed line is the height of the LCL.

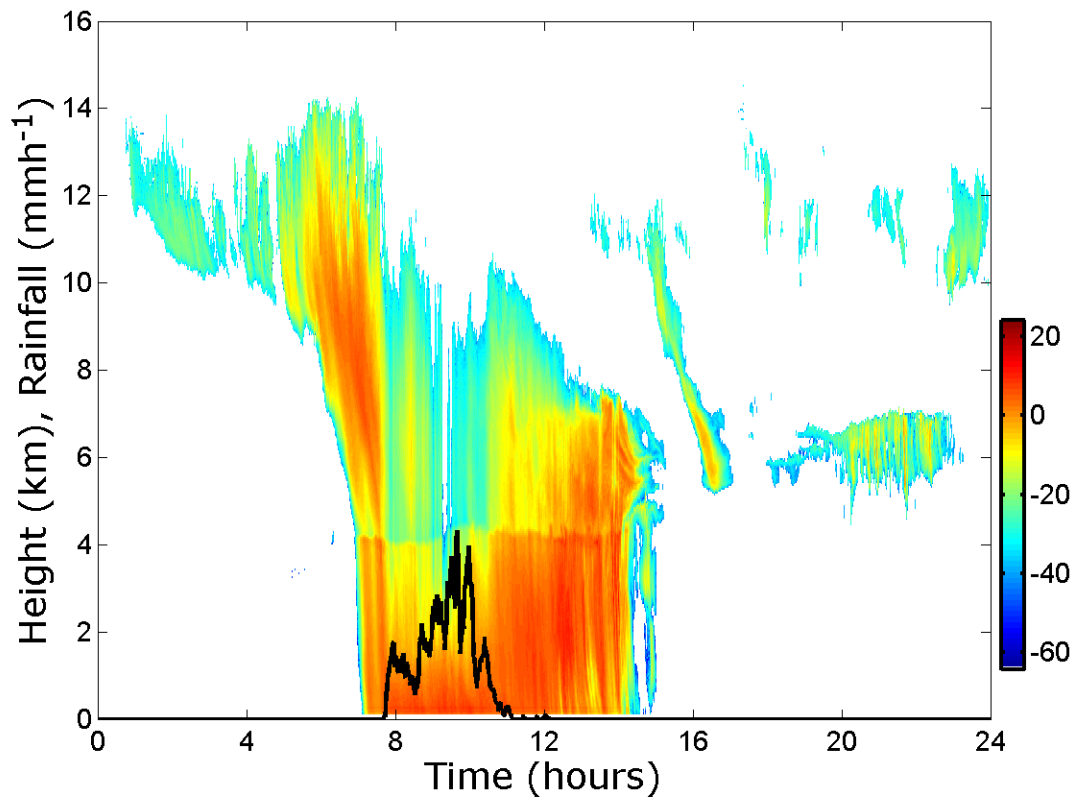
8

9 Figure 8. Relationships between monthly mean variables and the occurrence of clouds  
10 and intensity of precipitation for rainy season. (a-b) the monthly mean CAPE and LCL  
11 height versus the mean amount of rainfall likely to be observed during any individual  
12 event, The asterisk denotes the exclusion of November for these correlations. Inclusion  
13 reduces  $R^2$  for the LCL height to 0.62. Column Cloudiness Index and (c) monthly mean  
14 LCL, (d) monthly mean zero degree isotherm height, (e) monthly mean event  
15 precipitation, and (f) monthly mean event precipitation rate.

16

17

18



1

2

3

4

5

6 Fig. 1: Example of 94-GHz cloud radar reflectivity on August 8, 2006 at Niamey, Niger  
7 during the AMF deployment. The black line indicates the tipping bucket surface rainfall  
8 rate in mmh<sup>-1</sup>

9

10

11

12

13

14

15

16

17

18

19

20

21

22

23

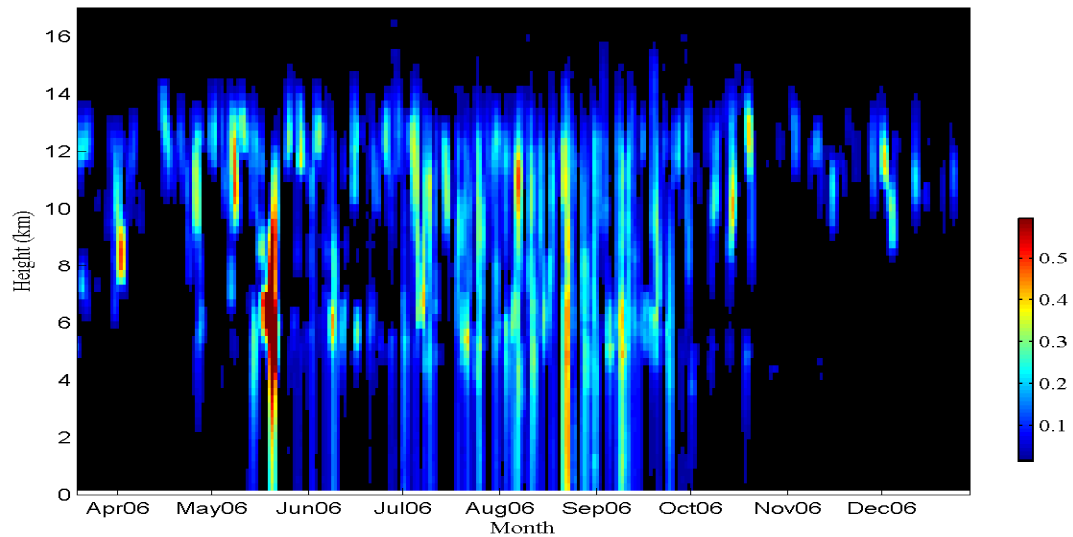
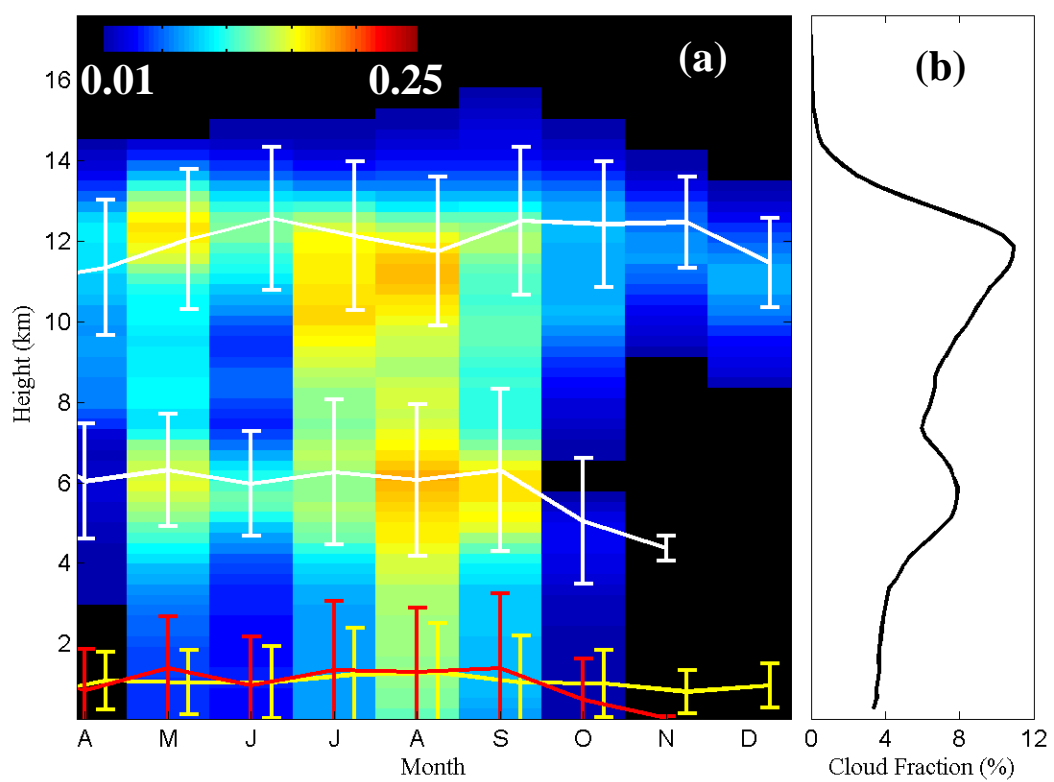
1  
23  
4  
5  
6  
7  
8  
9  
10  
11  
12  
13  
14  
15  
16  
17  
18  
19  
20  
21  
22  
23  
24  
25  
26  
27  
28  
29  
30

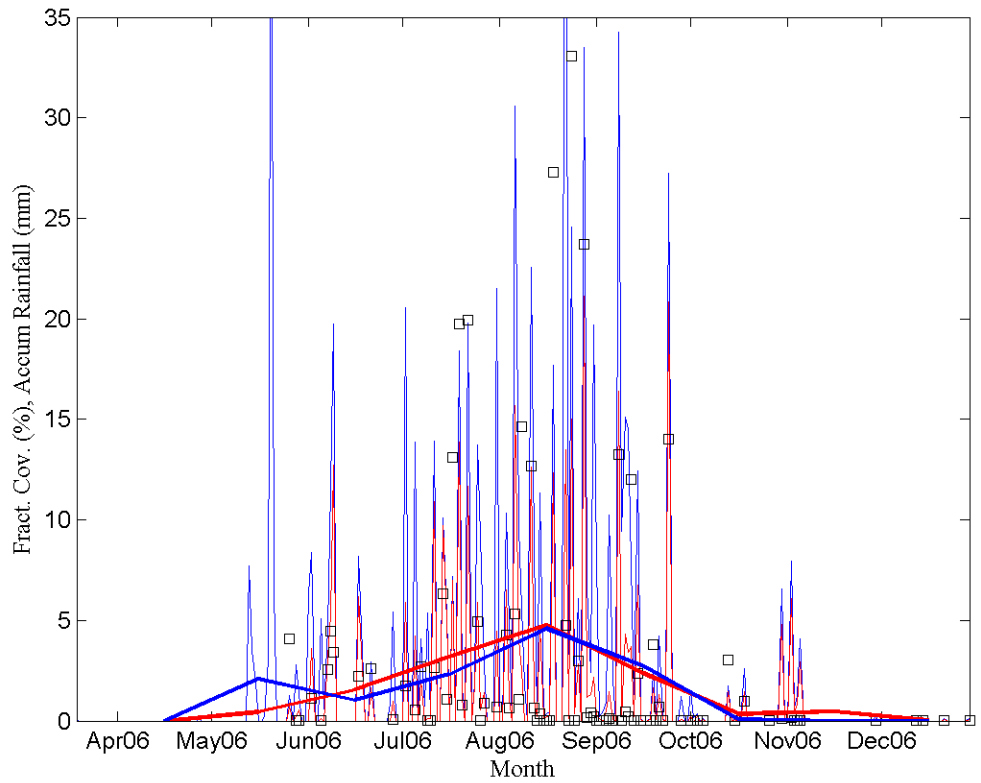
Fig. 2: Daily observed cloud fraction in Niamey during the AMF deployment. The cloud fraction is derived from measurements from the 94-GHz radar, the micro-pulse lidar and the ceilometer. The vertical resolution is 260 m and a 5-day temporal filter is applied to the daily cloud fraction profiles.



1  
2  
3  
4  
5  
6  
7  
8  
9  
10  
11  
12  
13  
14  
15  
16  
17  
18

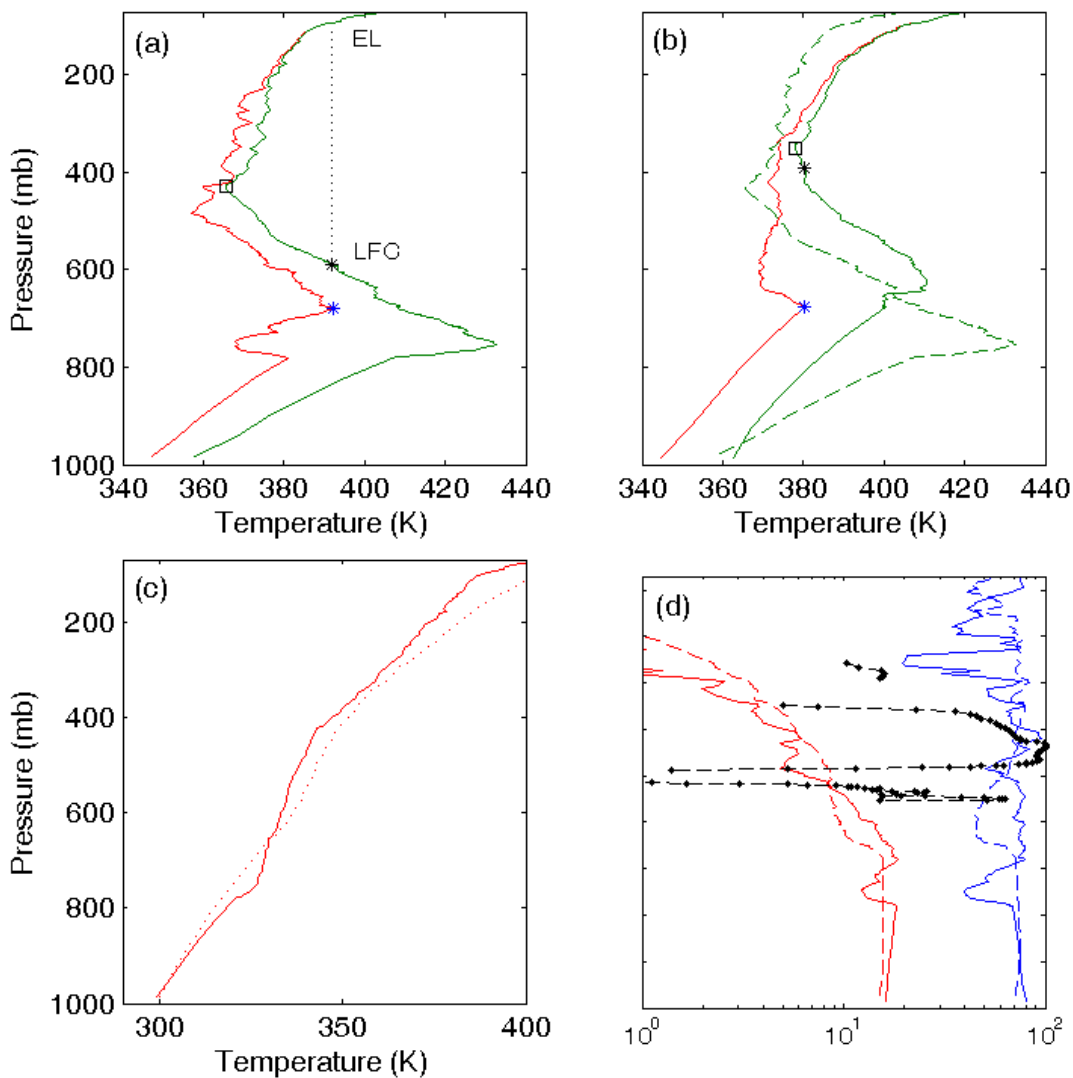
Fig. 3: (a) Monthly-averaged cloud and precipitation fraction. The monthly mean and standard deviation of cirrus cloud top (white line), middle clouds tops (white line), cirrus cloud thickness (yellow line) and middle clouds thickness (red) are also shown. (b) The deployment-mean cloud and precipitation fraction during the AMF deployment at Niamey, Niger.

1  
2  
3  
4  
5



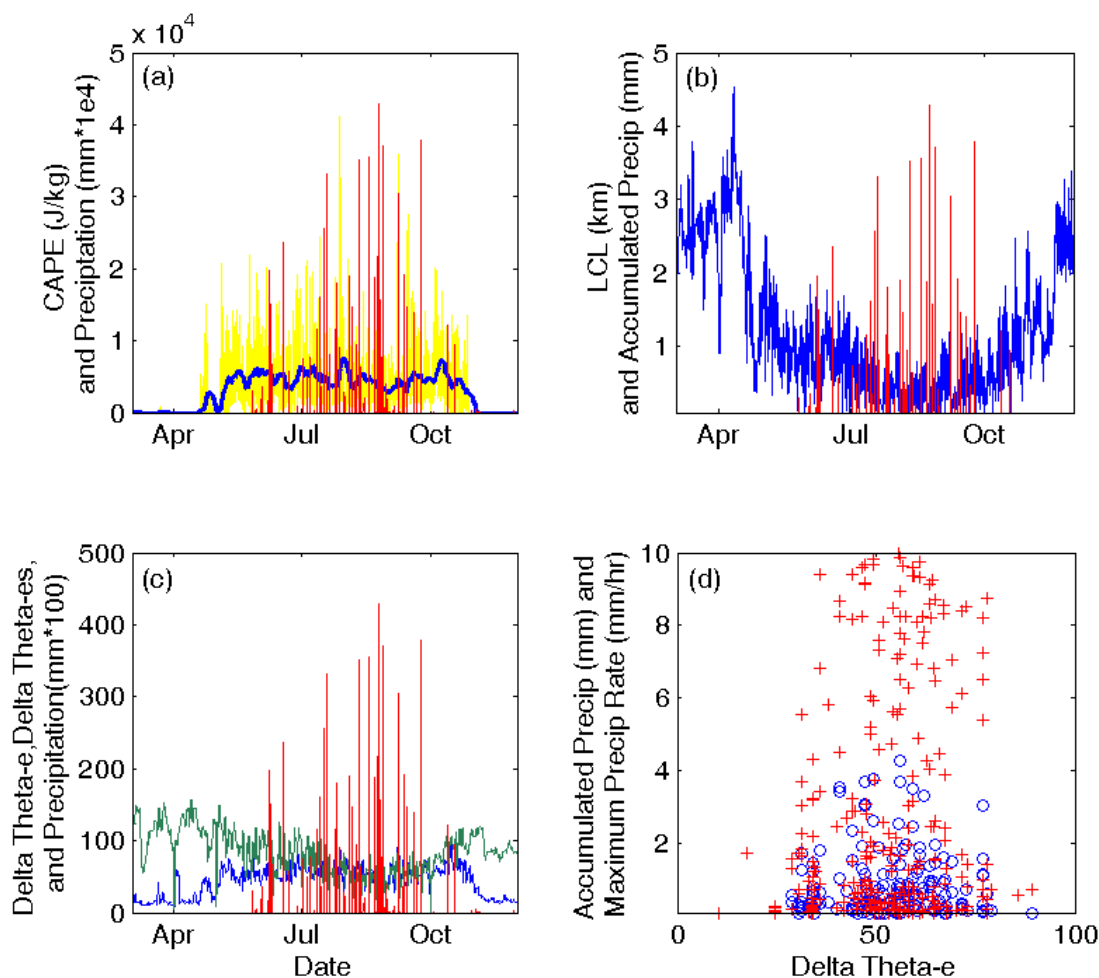
6  
7  
8  
9  
10  
11  
12  
13  
14  
15  
16  
17  
18  
19  
20

Fig. 4 Daily- and monthly-observed fractional coverage of precipitation (radar echo) (blue thin and thick lines), accumulated daily rainfall (in mm, black squares) and daily- and monthly-observed fractional coverage of measurable precipitation by the tipping bucket (rainfall > 0.245 mmh<sup>-1</sup>) at the AMF site.



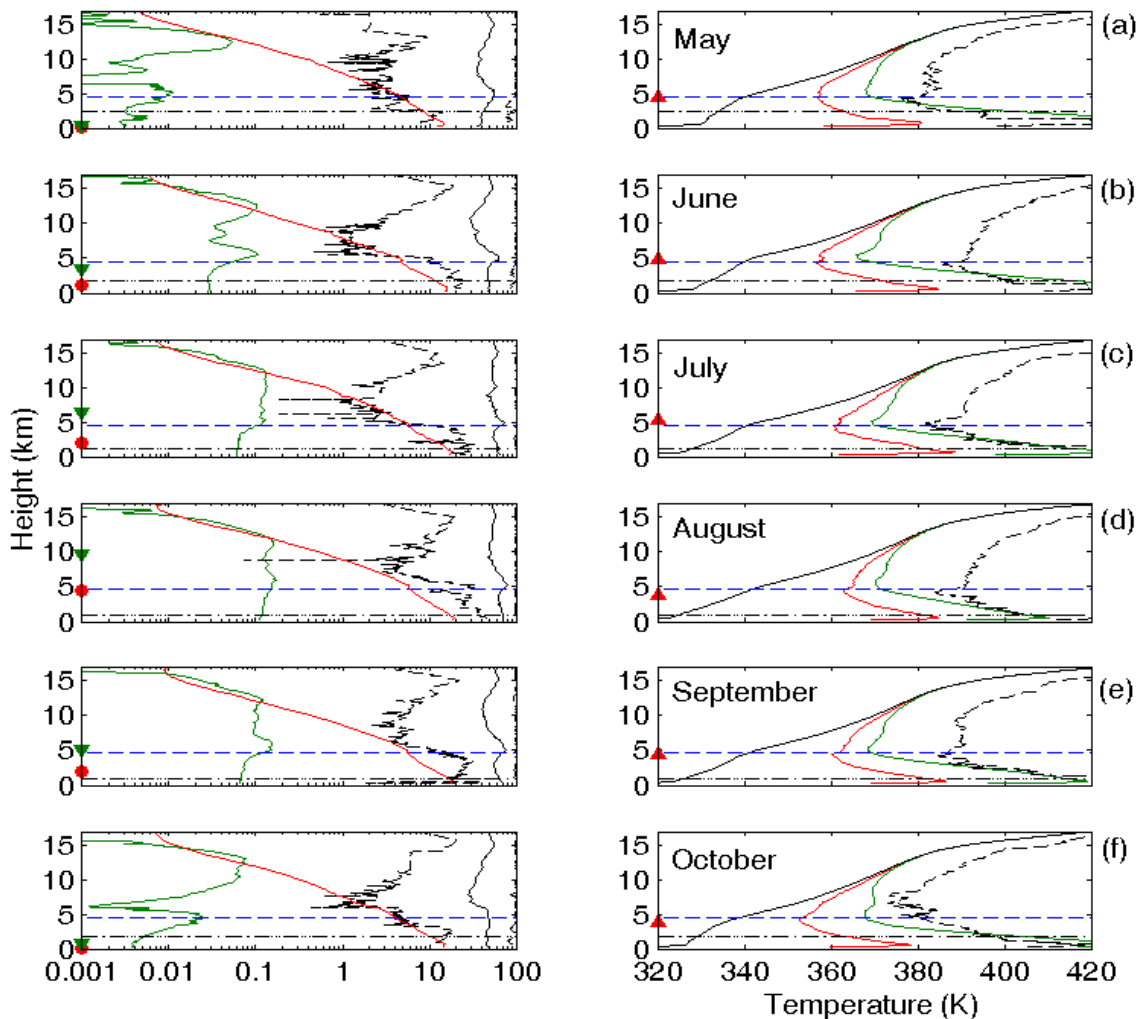
1  
2  
3  
4  
5  
6  
7  
8  
9  
10  
11  
12  
13  
14  
15  
16  
17

Figure 5. Pre- (0500 UTC) and post-storm (1300 UTC) environments for 9 June 2006. (a) The equivalent potential (red) and saturation equivalent potential temperatures (green) for the pre-storm environment. The Level of Free Convection (LFC) and Equilibrium Level (EL) are indicated and the blue asterisk and black square represent reference thermodynamic levels referred to in the text. The region bounded by the dashed black line and the green line is the positive area. (b) as in (a), but for the post-storm environment. The dashed green line is the saturation equivalent temperature from the pre-storm environment for reference. (c) The potential temperature profile for the pre- (solid) and post-storm environments. (d) The mixing ratio (red) and the relative humidity (blue) for the pre- (solid) and post-storm (dashed) environments. The black line with filled-circles is the non-zero percent coverage of clouds in the post-storm environment.

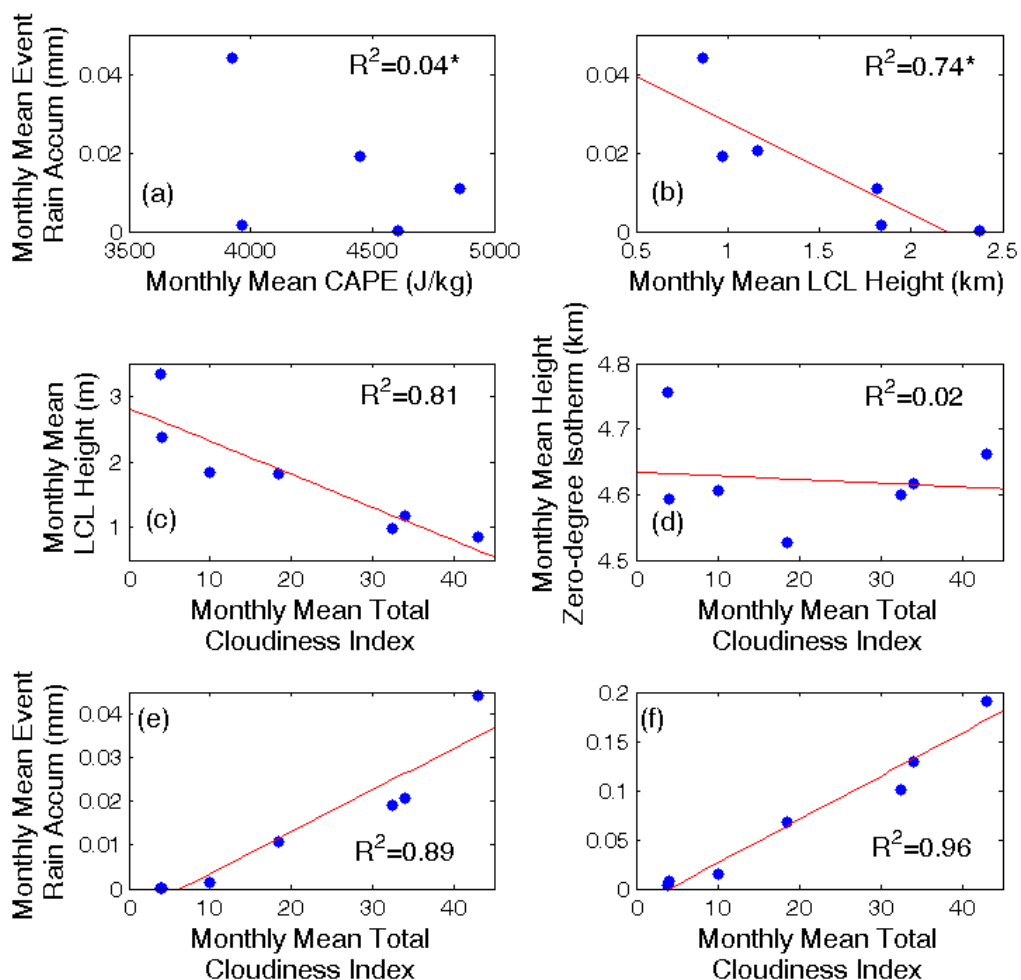


1  
2  
3 Figure 6. (a) The temporal relationship between CAPE and precipitation. The yellow line  
4 connects the half-hour estimations of CAPE and the blue line is a running mean through  
5 the raw CAPE estimates. The red lines are half-hour values of accumulated precipitation  
6 multiplied by  $1.0 \times 10^4$  for display convenience. (b) The half-hour average LCL (blue)  
7 versus accumulated precipitation (red). (c) Half-hour fluctuations in  $\theta_e$  and  $\theta_{es}$  versus  
8 accumulated precipitation multiplied by 100 for display convenience. (d) Half-hour  
9 accumulated precipitation and precipitation rate versus half-hour fluctuations in  $\theta_e$ .

10  
11  
12  
13  
14  
15  
16  
17  
18



1  
 2  
 3 Figure 7. (left column) Monthly mean profiles of cloud fractional coverage (green),  
 4 relative humidity (black), minimum relative humidity and maximum relative humidity  
 5 envelope (black dashed left and right of solid black line) for the months of May through  
 6 October (a-f). The monthly mean accumulation from individual precipitation events is  
 7 indicated with the filled red circle on the height axis and the monthly mean precipitation  
 8 rate from individual precipitation events is indicated with the inverted green triangle.  
 9 (right column) Monthly mean profiles of  $\theta$  (black),  $\theta_e$  (red),  $\theta_{es}$  (green), and minimum  $\theta_e$   
 10 (black dashed) and the monthly mean CAPE/1000 ( $\text{J kg}^{-1}$ ). (left and right columns) The  
 11 blue dashed line on each plot is the mean monthly level of the zero-degree isotherm and  
 12 the black dot-dashed line is the height of the LCL.  
 13  
 14



1  
2

3 Figure 8. Relationships between monthly mean variables and the occurrence of clouds  
4 and intensity of precipitation for rainy season. (a-b) the monthly mean CAPE and LCL  
5 height versus the mean amount of rainfall likely to be observed during any individual  
6 event, The asterisk denotes the exclusion of November for these correlations. Inclusion  
7 reduces  $R^2$  for the LCL height to 0.62. Column Cloudiness Index and (c) monthly mean  
8 LCL, (d) monthly mean zero degree isotherm height, (e) monthly mean event  
9 precipitation, and (f) monthly mean event precipitation rate.